

Article

Adsorption Performance and Mechanism of Fe(II) Adsorption in Abandoned Mine Water of Nonstick Coal

Zhuolin Shi ^{1,2}, Chengle Wu ^{1,2,*}, Furong Wang ^{1,2}, Jialong Sun ^{1,2}, Yingnan Xu ^{1,2} and Jinhang Shen ^{1,2}

¹ Key Laboratory of Deep Coal Resource Mining, Ministry of Education, School of Mines, China University of Mining and Technology, Xuzhou 221008, China; shizhuolin@cumt.edu.cn (Z.S.); wangfurong0511@126.com (F.W.); ts22020181p21@cumt.edu.cn (J.S.); xyn5426@163.com (Y.X.); ts22020053a31@cumt.edu.cn (J.S.)

² School of Mines, China University of Mining and Technology, Xuzhou 221116, China

* Correspondence: ts21020054a31@cumt.edu.cn

Abstract: Aiming at the problem of the low reuse rate of mine water due to the high content of heavy metals in mine water, in this research, the microcharacterization means of EDX, XRD, BET, SEM, and FT-IR were used to characterize the nonstick coal in a mine in western China. The effects of solid–liquid ratio, solution pH, solution temperature, adsorption time, and initial concentration of the solution on the adsorption of Fe(II) by the nonstick coal were analyzed. The adsorption performance of nonstick coal on adsorbed Fe(II) was analyzed under different influencing factors. The results showed that the adsorption capacity and unit removal rate of the coal samples gradually decreased with the increase in the solid–liquid ratio; the adsorption amount increased with the increase in pH in an “S” shape, and the adsorption effect was better in the range of pH = 5–7; and the adsorption amount increased linearly with the temperature. The quasi-secondary kinetic model and Langmuir model could fit the adsorption kinetic curve and isothermal adsorption curve better, which indicated that the adsorption of Fe(II) by the nonstick coal was dominated by the chemical adsorption of the monomolecular layer. The quantitative analysis of the FT-IR results showed that the adsorption of Fe(II) was mainly by complexation with -OH detached from the coal samples to produce precipitation.

Keywords: mine water; heavy metal ion; nonstick coal; adsorption performance; adsorption mechanism



Citation: Shi, Z.; Wu, C.; Wang, F.; Sun, J.; Xu, Y.; Shen, J. Adsorption Performance and Mechanism of Fe(II) Adsorption in Abandoned Mine Water of Nonstick Coal. *Processes* **2024**, *12*, 188. <https://doi.org/10.3390/pr12010188>

Academic Editors: Gujie Qian, Weifeng Chen and Yan Zhou

Received: 22 November 2023

Revised: 7 January 2024

Accepted: 9 January 2024

Published: 15 January 2024



Copyright: © 2024 by the authors. Licensee MDPI, Basel, Switzerland. This article is an open access article distributed under the terms and conditions of the Creative Commons Attribution (CC BY) license (<https://creativecommons.org/licenses/by/4.0/>).

1. Introduction

The western mining region (Shanxi, Shaanxi, Inner Mongolia, Gansu, and Ningxia) is the main production area for coal mining in China. In 2022, raw coal production in the western mining region of China accounted for more than 70% of China’s total production [1]. However, water resources in the ecologically fragile western mining areas are relatively scarce. The total amount of water resources accounts for only 6.66 percent of the national total. So, the contradiction of coal–water mining is very prominent. Coal mining destroys the overlying rock structure, causing surface subsidence, water table decline, soil erosion, and vegetation destruction, further exacerbating the loss of water resources in the region [2,3]. Therefore, some scholars have proposed storing mine water in the coal mining airspace to form an underground water reservoir for the purpose of protecting and utilizing water resources [4,5]. However, the content of heavy metal elements in mine water is too high. There are significant environmental and health risks. It also reduces the possibility of reuse of mined water and decreases the efficiency of utilization [6–9]. The standard heavy metal ions in mine water include Cr(VI), Cd(II), Fe(II), Mn(II), and Ni(II) [10]. Among them, Fe(II) is one of the heavy metal ions with a high content in mined Jurassic coal seams in western China [8,9]. Standard treatment methods for heavy metal ions in mine water include wetland treatment, neutralization, microbiological methods, and adsorption [11,12]. Among them, the adsorption method is considered a cost-effective

and highly applied treatment method because of its advantages of good treatment effects, a comprehensive source of materials, energy-saving economics, and simple operation [13,14]. The natural adsorbents available in groundwater reservoirs are mainly mined-area rocks and coal left after mining. There are abundant studies on using mined-area rocks for heavy metal adsorption.

Reference [15] investigated the adsorption characteristics of different types of lignite for Cu, Zn, Pb, Cd, Ni, Co, and Fe(II) ions, and the results showed that lignite has potential for water pollution treatment. Reference [16] investigated the suitability of Ukrainian lignite as an adsorption detoxifier for heavy metal-contaminated soils. The results indicate that lignite has a higher capacity to adsorb heavy metals due to its large specific surface area and the presence of functional groups that ensure the chemisorption of pollutant cations. Reference [17] investigated the adsorption properties of sandy mudstone and fine sandstone from gangue in a mining area on Mn(II) in mine water. The adsorption properties increased with the increase in temperature, pH, and solid–liquid ratio. Reference [18] adsorbed Cr(VI) through modified gangue, designed adsorption experiments to investigate the adsorption performance, and explored the adsorption mechanism by combining XRF, TG-DSC, XRD, and SEM analytical characterization means. The results showed that the adsorption process and isothermal adsorption curves conformed to the quasi-secondary kinetic equation and the Freundlich model.

Most scholars have investigated the adsorption of heavy metal ions by rocks in mining areas. At the same time, more research needs to be performed on the adsorption properties of coal left in mining areas. Due to the characteristics of coal with a large specific surface area and containing clay minerals, it also contains active groups that can easily undergo coordination complexation and ion exchange reactions with metal ions. These characteristics have great potential for the adsorption of heavy metal ions in mine water. Therefore, the adsorption performance and adsorption mechanism of Fe(II) were investigated using the leftover nonstick coal in a mine.

2. Experimental Section

2.1. Experimental Materials

Coal samples: Nonstick coal was taken from the remaining coal in the goaf area of a coal mine in western China. The mined seam thickness was 5.98 m, using comprehensive mechanized coal mining with a high recovery rate of 97%. The coal samples' natural and saturated moisture contents were 6% and 4.3%, respectively. Nonstick coal fragments were retrieved from the site, grinding tools were used to crush them into coal powder, and the coal powder was screened out with a particle size of 200 mesh for backup.

Fe(II) solution preparation: The $\text{FeCl}_2 \cdot 4\text{H}_2\text{O}$ solid was dissolved in HCl at a concentration of 1 mol L^{-1} and stirred with a glass rod. After the solid was completely dissolved, the Fe(II) concentration was diluted to 1 mg mL^{-1} by adding secondary deionized water to make an initial solution of Fe(II). When the target solution was needed, the initial solution of Fe(II) was diluted with secondary deionized water and the pH value of the solution was adjusted using HCl and NaOH. The pH value of the solution was measured using a laboratory pH meter (PHS-3C type, Instruments & Electronics (Shanghai) Association, Shanghai, China). All chemicals and reagents used in this experiment were analytical grade.

2.2. Coal Sample Characterization

The pathway for the coal sample characterization test is shown in Figure 1. The study of heavy metal ions' adsorption performance and adsorption mechanism for coal samples requires an understanding of their composition, surface morphology, pore distribution, and molecular structure. Coal samples before and after adsorption were analyzed by X-ray diffraction (XRD) using a Rigaku D/Max-II B (Bruker, Berlin, Germany) diffractometer to obtain their mineral fractions, and the diffraction angle step was 0.05° during the test. The elemental analyzer Vario EL cube (Elementar GMBH, Frankfurt, Germany) was used to determine the elemental composition and content (EDX) of the coal samples before and

after adsorption. An S-4800 (HITACHI, Tokyo, Japan) scanning electron microscope (SEM) was used to capture images of the coal samples before and after adsorption. The test voltage and current were 3 kV and 10 μ A, respectively. Measurement of the pore structure of the coal samples before adsorption was performed using a fully automatic specific surface area and microporous physical adsorption instrument (Micromeritics, ASAP-2020 HD-88, Atlanta, GA, USA). The specific surface area (BET), Barrett–Joyner–Halenda (BJH) pore size distribution, and pore size parameters of the coal samples before adsorption were determined using a specific surface area analyzer (ASAP2020HD88). A Shimadzu Model 1.50SU1 was used to measure the coal samples' Fourier transform infrared transmission spectroscopy (FT-IR) with a 400–4000 cm^{-1} measurement wavelength range.

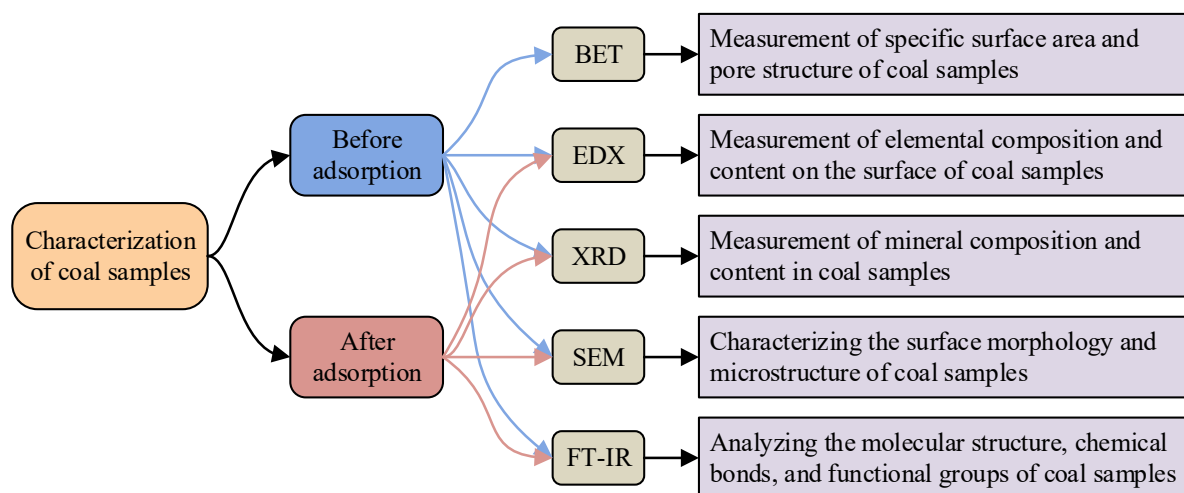


Figure 1. Coal sample characterization test roadmap.

2.3. Adsorption Experiment

Design isothermal adsorption experiments with different pH values to study the effect of pH changes on Fe(II) adsorption by coal samples. Add 1 g of coal sample to 20 mL of 10 mg L^{-1} Fe(II) solution, and the pH value of the solution varies between 2 and 7. Design isothermal adsorption experiments with different solid–liquid ratios to study the effect of changes in the solid–liquid ratio on the adsorption of Fe(II) by coal samples. Add different-quality coal samples into 50 mL 10 mg L^{-1} Fe(II) solution, and the quality of coal samples changes in the 1–3 g range. Design adsorption thermodynamic experiments to study the effect of temperature changes on Fe(II) adsorption on coal samples. Add 1 g of coal sample to 20 mL of 10 mg L^{-1} Fe(II) solution, and the solution temperature varies between 25 and 55 $^{\circ}\text{C}$. Add 1 g of coal sample to 20 mL of 10 mg L^{-1} Fe(II) solution and conduct adsorption kinetics experiments within 1–24 h. The isothermal adsorption test involves adding 1 g of coal sample to 20 mL of Fe(II) solution, with an initial Fe(II) concentration ranging from 1 to 50 mg L^{-1} . The above tests were performed on a horizontal shaker. Immediately after reaching the corresponding adsorption time, take the upper clear liquid for Fe(II) concentration detection. Meanwhile, filter out the coal sample with filter paper and place it in a drying oven to dry at 105 $^{\circ}\text{C}$ for 4 h. The nonvariable parameters and variable parameter gradients in each experiment are shown in Table 1.

2.4. Determination of Fe(II) Concentration

In this experiment, o-phenanthroline spectrophotometry was used to precisely detect the concentration of Fe(II) in solution [19]. The tested solution was first diluted by adding 1 mL to the test tube. Second, 0.15% (g mL^{-1}) phenanthroline, 0.10% (g mL^{-1}) hydroxylamine hydrochloride, and 8.23% (g mL^{-1}) sodium acetate were added to the test tube in that order. Finally, water was added to 10 mL, followed by 10 min of waiting time. A suitable volume of liquid was put into a 10 mm colorimetric dish and was measured by a

UV spectrophotometer (HACH/DR5000) with the absorbance at 510 nm. The adsorption capacity (q , mg g^{-1}) and unit removal rate ($A\%$) of absorbed Fe(II) were estimated using Equations (1) and (2):

$$q = \frac{(C_0 - C_e) \times V}{m} \quad (1)$$

$$A(\%) = \frac{C_0 - C_e}{mC_0} \times 100\% \quad (2)$$

where V is the volume (L) of the Fe(II) solution; m is the mass (g) of the coal sample; and C_0 and C_e represent the initial and equilibrium concentration of Fe(II) in the solution (mg L^{-1}), respectively.

Table 1. Adsorption experimental parameters.

Experiment Name	pH	Solid-Liquid Ratio (g mL^{-1})	Temperature ($^{\circ}\text{C}$)	Time (h)	Concentration (mg L^{-1})
Isothermal adsorption experiments with different pH values	2, 3, 4, 5, 6, 7	1:20	25	2	10
Isothermal adsorption experiments with different solid-liquid ratios	6	1:50, 1.5:50, 2:50, 2.5:50, 3:50	25	0.5, 2	10
Adsorption thermodynamics experiment	6	1:20	25, 35, 45, 55	5	10
Isothermal adsorption experiment	6	1:20	25	24	1, 4, 8, 10, 12, 16, 20, 25, 30, 40, 50
Adsorption kinetics experiment	6	1:20	25	0-24	10

A standard curve for this test method is required to determine the concentration of Fe(II) in a solution after adsorption. Standard Fe(II) solutions with concentrations of 1 mg L^{-1} , 2 mg L^{-1} , 5 mg L^{-1} , 10 mg L^{-1} , 15 mg L^{-1} , and 20 mg L^{-1} were configured, and the absorbance of the solutions was tested. The standard curve obtained is shown in Figure 2.

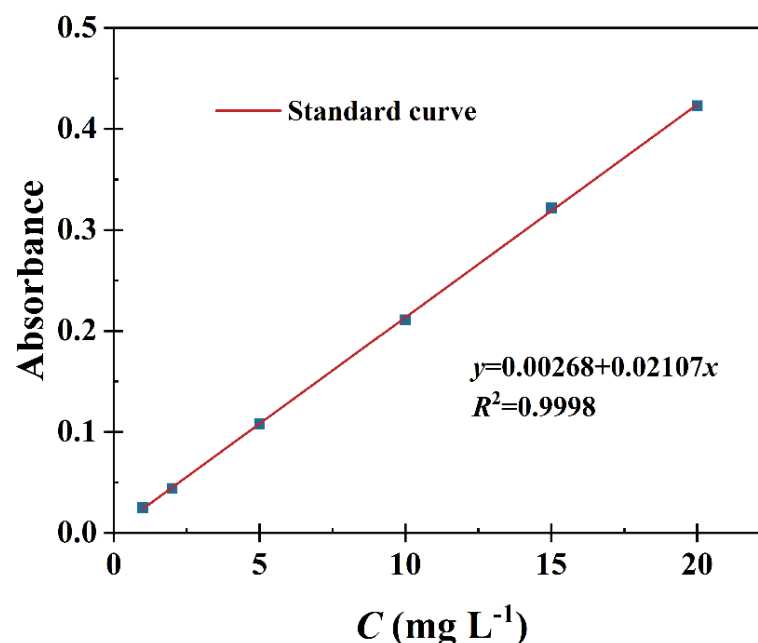


Figure 2. Standard curve of Fe(II).

3. Results and Discussion

3.1. Characterization of Nonstick Coal

The chemical element composition of the nonstick coal was quantitatively analyzed by the EDX method, and the results are shown in Figure 3a. The spectrum shows that the

chemical elements contained in the nonstick coal are mainly C, O, Al, Si, S, and Ca. The percentages are 77.18%, 19.62%, 0.13%, 0.16%, 0.11%, and 2.80%, respectively.

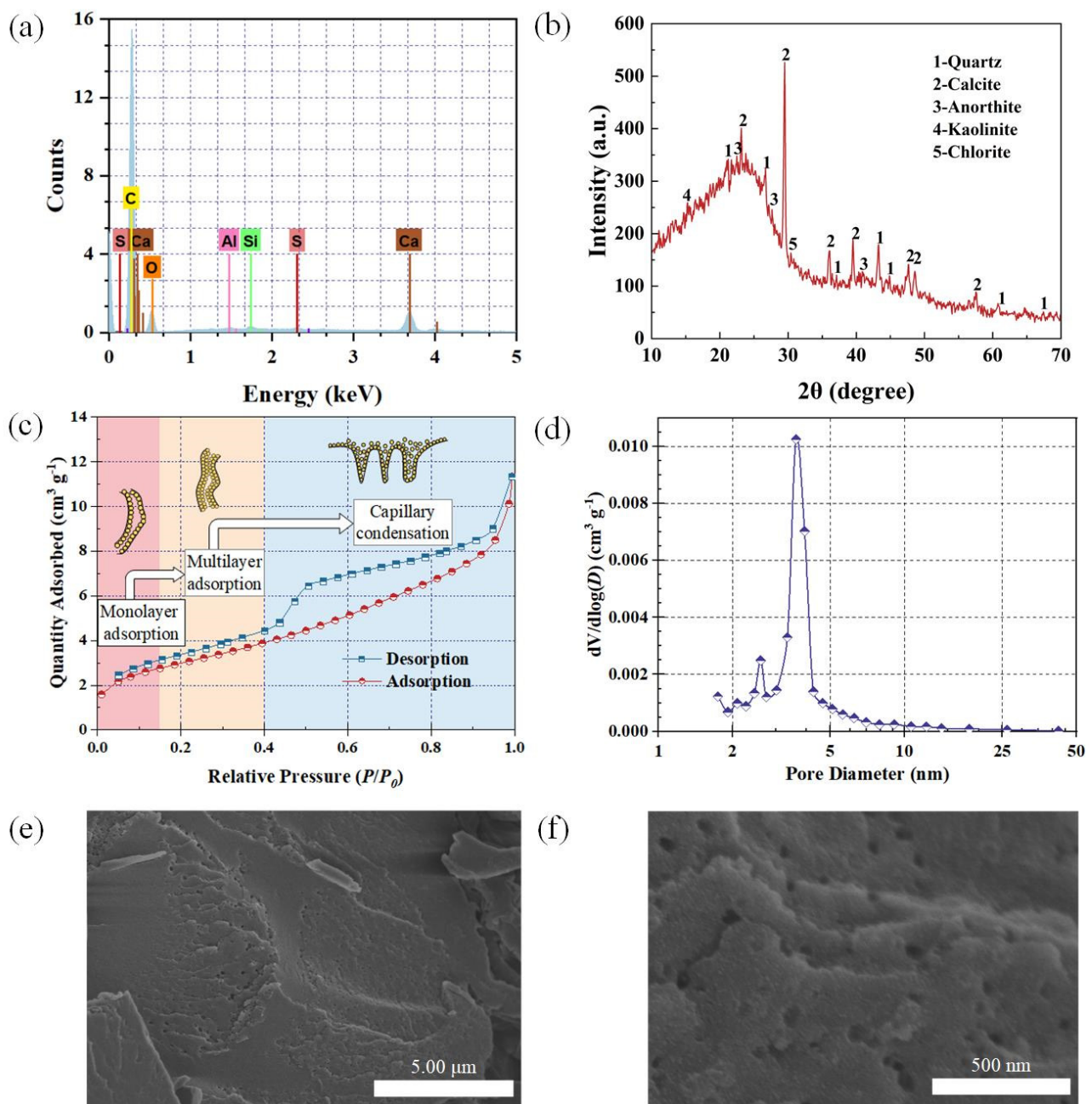


Figure 3. Characterization of nonstick coal. (a) EDX energy spectrum of nonstick coal. (b) XRD diffraction pattern of nonstick coal. (c) Nitrogen adsorption–desorption isotherm. (d) Aperture distribution of BJH. (e,f) SEM images of nonstick coal at 5.00 μm and 500 nm.

The X-ray diffraction results of the nonstick coal are shown in Figure 3b. Combined with EDX elemental measurements to quantitatively analyze the XRD patterns, it can be concluded that the main mineral components in the coal samples are quartz, calcite, calcium feldspar, and clay minerals. The clay minerals mainly include chlorite and kaolinite. The significant mineral mass fractions in the coal samples are shown in Table 2.

Table 2. Mineral mass fraction of nonstick coal.

Sample	Mineral Composition Analysis			Clay Mineral Analysis		
Coal sample	Quartz 27.6%	Calcite 42.6%	Anorthite 16.4%	Clay 13.4%	Chlorite 13%	Kaolinite 87%

The nitrogen adsorption–desorption isotherm of the coal samples is depicted in Figure 3c. According to the curve morphology, the coal samples consist of a typical mesoporous material that matches the Type IV isotherm and the Type H3 hysteresis ring [20] of the IUPAC’s categorization of porous solids. Monomolecular layer adsorption occurred in the micropores in the low relative pressure interval ($P/P_0 < 0.15$). As the relative pressure increased ($P/P_0 = 0.15–0.4$), multilayer adsorption occurred in some micropores, with minimal adsorption in this pressure interval. At high relative pressure ($P/P_0 > 0.4$), capillary coalescence occurred in the mesopores of the coal samples. Figure 3d shows the pore size distribution curve of the coal samples. According to the IUPAC pore size classification method, the pore sizes of the coal samples can be classified as microporous (less than 2 nm), mesoporous (2–50 nm), and macroporous (larger than 50 nm), which accounted for 12.7%, 85.8%, and 1.5%, respectively. Among them, the mesopores were mainly concentrated in the 2–10 nm range. The coal samples had a BET surface area of $10.724 \text{ m}^2 \text{ g}^{-1}$ and a pore volume of $0.013 \text{ cm}^3 \text{ g}^{-1}$. The average pore diameter determined by the BJH model was 5.265 nm, further demonstrating the mesoporous nature of the coal sample material.

Figure 3e,f show SEM images of the nonstick coal at different observation scales. The structure is dense, and the surface is relatively flat at the $5.00 \mu\text{m}$ observation scale, and its many tiny pore structures can be observed at the 500 nm observation scale. These pores increase the contact area between the coal sample and the liquid, which provides the basis for the adsorption of Fe(II).

3.2. Influence of pH on Adsorption of Fe(II) in Coal Samples

According to the literature, it is necessary to research the impact of pH change on the adsorbed Fe(II) in coal samples because some coal mines have acidic mine water [21,22]. The adsorption capacity of Fe(II) on coal samples under different pH values is shown in Figure 4. The experimental results showed that the adsorption of Fe(II) on coal samples increased with the increase in pH value in an “S” shape. The amount of coal sample adsorbed at pH = 2 is only 0.0043 mg g^{-1} . The adsorption of the coal sample rises to 0.0263 mg g^{-1} at pH = 4. The coal samples’ adsorption rises rapidly to 0.1724 mg g^{-1} at pH = 5. The coal samples’ adsorption rises to 0.1928 mg g^{-1} when the pH is 7. The experimental results show that there is a competitive adsorption relationship between H^+ and Fe(II) in the solution, leading to a decrease in the adsorption amount of Fe(II), since the adsorption sites in the coal samples tend to undergo a protonation reaction with H^+ at lower pH levels, which leads to a decrease in the number of adsorption sites.

3.3. Influence of the Solid–Liquid Ratio on Adsorption of Fe(II) in Coal Samples

Figure 5 shows the effect of coal samples on the adsorption capacity and unit removal rate of Fe(II) under different solid–liquid ratio conditions. Figure 5a shows the results after 0.5 h of adsorption. It can be seen that with the increase in the solid–liquid ratio, the adsorption capacity of the coal samples for Fe(II) increased linearly from 0.078 mg g^{-1} to 0.115 mg g^{-1} , and the corresponding unit removal rate increased linearly from 15.6% to 23.1%. Figure 5b shows the results after 2 h of adsorption. It can be seen that with the increase in the solid–liquid ratio, the adsorption capacity of the coal samples for Fe(II) decreased linearly from 0.198 mg g^{-1} to 0.148 mg g^{-1} , and the corresponding unit removal rate decreased linearly from 39.7% to 29.6%. With the same Fe(II) concentration at the beginning of adsorption (0.5 h), the active sites on the surface of solid particles increased accordingly with the increase in the solid–liquid ratio. Fe(II) in the solution was rapidly adsorbed by the adsorption sites on the surface of the particles before it diffused into the

interior of the coal sample particles. Therefore, the adsorption capacity and unit removal rate increased with the increase in the solid–liquid ratio. With the increase in adsorption time (2 h), the concentration of Fe(II) in the solution with a relatively sizeable solid–liquid ratio decreased, which led to the decrease in the adsorption capacity and unit removal rate of the coal samples with the increase in the solid–liquid ratio.

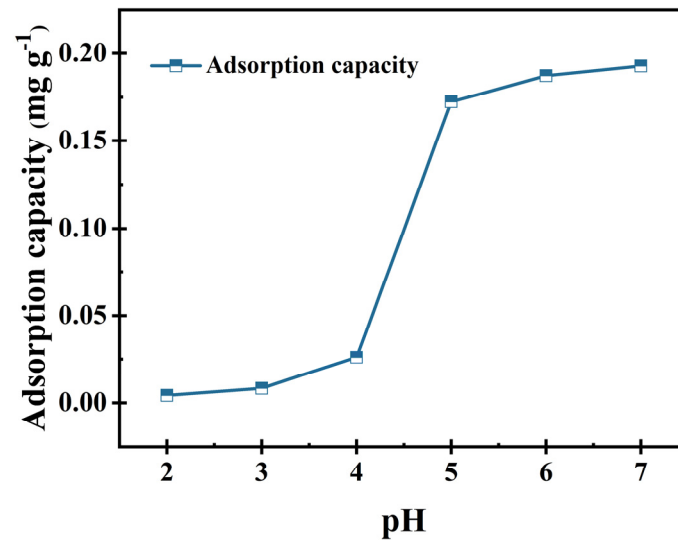


Figure 4. Effect of pH on Fe(II) adsorption from coal samples.

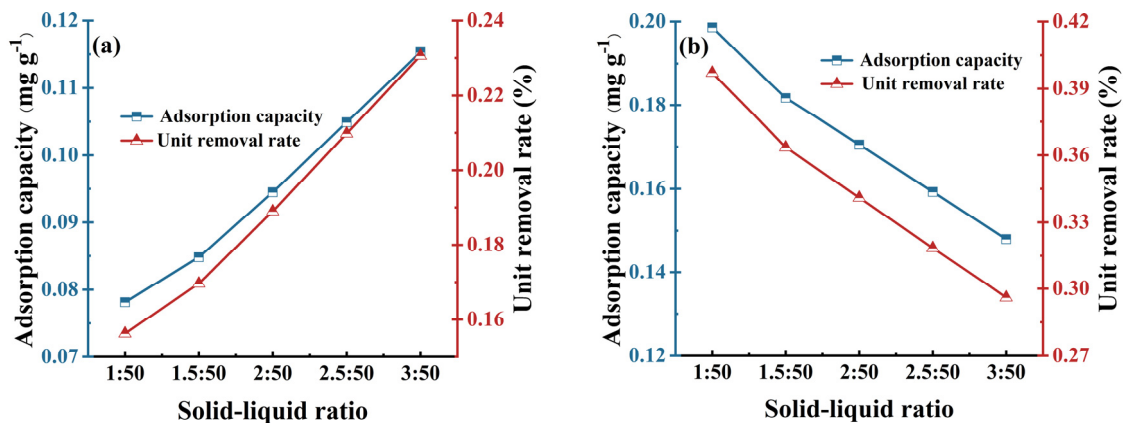


Figure 5. Effect of solid–liquid ratio on adsorption of Fe(II) on coal samples: (a) adsorbed for 0.5 h; (b) adsorbed for 2 h.

3.4. Thermodynamic Study of Adsorption

The effect of temperature change on the adsorption of Fe(II) from the coal samples is shown in Figure 6a. As the solution temperature increased from 25 °C to 55 °C, the adsorbed amount of the coal samples gradually increased from 0.168 mg L⁻¹ to 0.189 mg L⁻¹ with an increase of 12.5%, which indicates that the high-temperature environment is favorable for adsorption.

The enthalpy change (ΔH), Gibbs free energy (ΔG), and entropy change (ΔS) of the coal samples during adsorption of Fe(II) at 25–55 °C were calculated according to Equations (3)–(6), and the results are shown in Table 3. In the adsorption process, $\Delta H > 0$ indicates that the adsorption of Fe(II) from coal samples is heat-absorbing, suggesting that raising the temperature is favorable for adsorption; $\Delta G > 0$ and decreases gradually with

increasing temperature, suggesting that heating is favorable for the adsorption of heavy metal ions and that the adsorption reaction proceeds spontaneously.

$$D = \frac{q_e}{C_e} \quad (3)$$

$$\Delta G = -RT \ln D \quad (4)$$

$$\Delta G = \Delta H - T\Delta S \quad (5)$$

$$\ln D = -\frac{\Delta H}{RT} + \frac{\Delta S}{R} \quad (6)$$

where q_e stands for the degree of adsorption at the appropriate temperature when the adsorption process reaches equilibrium (mg g^{-1}); T is the absolute temperature (K); R is the thermodynamic constant ($\text{J mol}^{-1} \text{K}^{-1}$); C_e is the concentration of Fe(II) in the solution at equilibrium (mg g^{-1}); and D is the adsorption equilibrium constant.

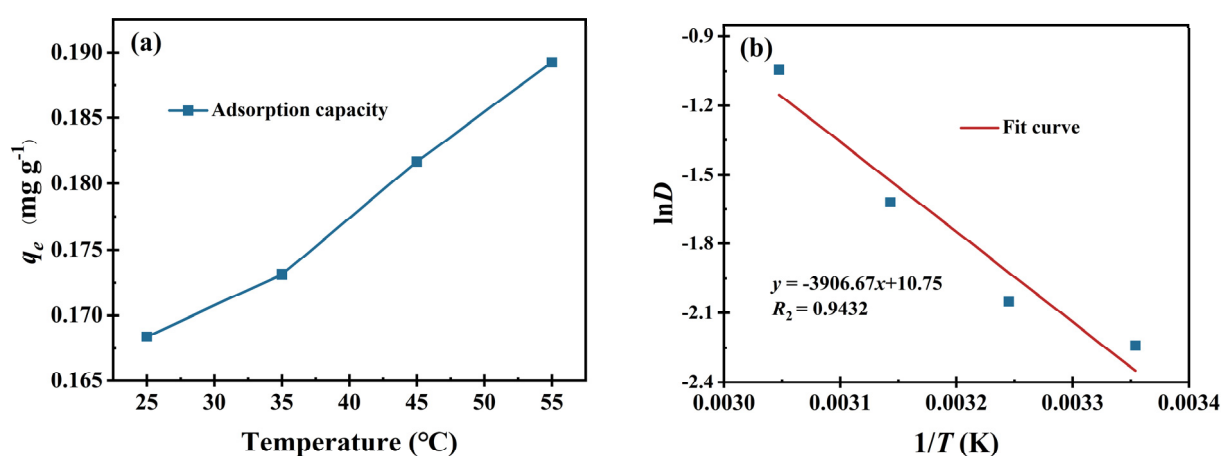


Figure 6. (a) Influence of temperature on adsorption of Fe(II) on coal samples. (b) The fitting curve between $\ln D$ and $1/T$.

Table 3. The thermodynamic parameters of Fe(II) adsorption on coal samples at different temperatures.

T (K)	ΔG (kJ mol^{-1})	ΔS ($\text{J mol}^{-1} \text{K}^{-1}$)	ΔH (kJ mol^{-1})
298	5.55	89.40	32.21
308	5.25	89.40	32.80
318	4.28	89.40	32.73
328	2.85	89.40	32.18

3.5. Adsorption Dynamic Curves and Equations

The adsorption process is generally categorized into three processes [23,24]: the external diffusion process, the internal diffusion process, and the surface adsorption process. The speed of the adsorption process to reach the equilibrium time can reflect the adsorption efficiency of coal samples. The adsorption kinetic experiments were carried out according to the solution and coal sample parameters in Table 1, and the results are shown in Figure 7a. It can be seen that the adsorption capacity of Fe(II) from coal samples with the increase in time went from a rapid increase in the early stage to a gradual decrease in the late stage, and the adsorption capacity was in an exponential curve with time. In 0–3 h, most of the Fe(II) in the solution was adsorbed by the coal sample, and the adsorption capacity was as high as 93.4%. The increase in the adsorption amount was not apparent with the increase in time, and the adsorption tended to equilibrium at 5 h. In order to ensure the complete adsorption equilibrium, the longest adsorption time was extended to 24 h. As porous media, the pore

sizes and surface areas of the coal samples are relatively large, exposing many adsorbable sites. Since the solution is mainly on the outer surface of the coal sample particles at the early adsorption stage, the adsorption process is external diffusion and surface adsorption. Since there are more adsorption sites on the outside of the coal particles than on the inside, the coal samples quickly absorb a large amount of Fe(II). With the increase in time, the adsorption capacity and the adsorption rate decreased due to the decrease in the adsorbable active sites and the change of the adsorption process to the internal diffusion process.

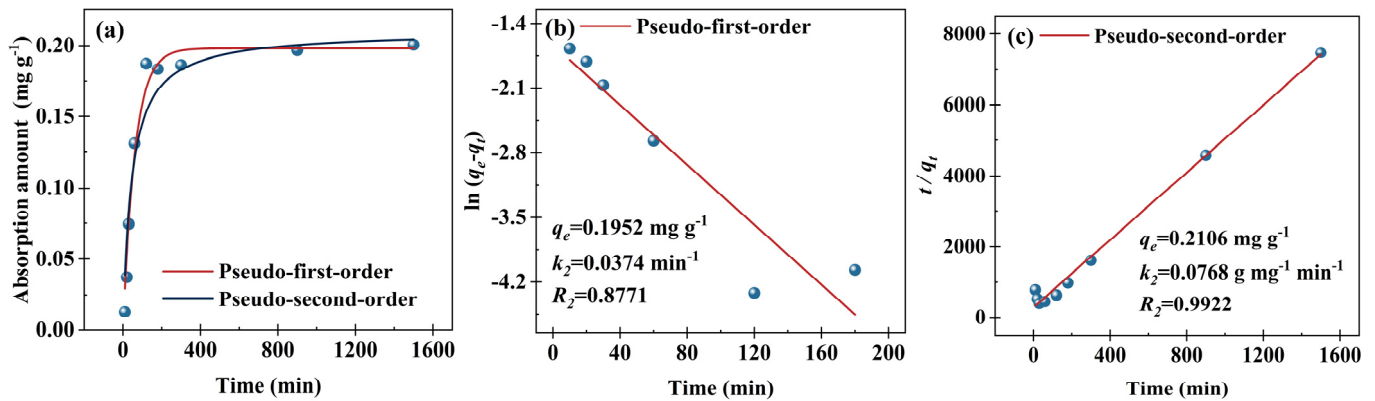


Figure 7. (a) Adsorption kinetics of Fe(II) on coal samples. (b) Pseudo-first-order kinetic model and (c) pseudo-second-order kinetic model from (a).

In order to estimate the adsorption rate and investigate the adsorption mechanism, the quasi-first-order dynamic model [25] and quasi-second-order dynamic model [26] are typically employed to fit adsorption data. The quasi-first-order dynamic model and quasi-second-order dynamic model are expressed in Equations (7) and (8).

$$\ln(q_e - q_t) = \ln q_e - \frac{k_1 t}{2.303} \quad (7)$$

$$q_t = \frac{q_e^2 k_2 t}{1 + q_e k_2 t} \quad (8)$$

where q_e and q_t represent the amount of adsorption at equilibrium and the instantaneous adsorption at time t (mg g^{-1}), respectively, and k_1 and k_2 are the adsorption rate constants of the quasi-first-order kinetic equation (min^{-1}) and the quasi-second-order kinetic equation ($\text{g mg}^{-1} \text{min}^{-1}$), respectively. Figure 7b. Plotting t through $\ln(q_e - q_t)$ computes q_e and k_1 (see Figure 7b). Plotting against t via t/q_t calculates q_e and k_2 (see Figure 7c). The results show that the pseudo-second-order model can better describe the adsorption behavior of Fe(II) on coal samples because the R^2 of the pseudo-second-order fitting is higher than that of the pseudo-first-order fit, which indicates that the adsorption is mainly dominated by chemisorption.

3.6. Isothermal Adsorption Curve Analysis

Table 1 lists the solution and coal sample parameters for the isothermal adsorption experiments, which were designed to investigate the adsorption properties of coal samples for Fe(II) at different initial concentrations. The Langmuir [27] and Freundlich [28] adsorption isothermal models are usually used to analyze experimental data by nonlinear curve fitting, which can provide an understanding of the strength of the adsorption, the characteristics of the adsorbed molecules, and the changes in the structure of the adsorbed layer.

The Langmuir equation is the ideal theory of adsorption in a single molecular layer, which indicates that the adsorption sites are uniformly distributed on the surface of the

adsorbent and that the molecules do not interact with each other during the adsorption process. The exact expression is given in Equation (9).

$$q_e = \frac{bq_m C_e}{1 + bC_e} \quad (9)$$

where q_e represents the adsorption capacity when the adsorption process reaches a balance at the corresponding concentration (mg g^{-1}); C_e is the concentration of adsorbent in the solution at the adsorption equilibrium (mg L^{-1}); q_m is the saturated adsorption capacity of the adsorbent (mg g^{-1}); and b is the Langmuir equilibrium adsorption characteristic constant, which can represent the strength of the adsorption capacity.

The Freundlich equation is a multimolecular layer adsorption theory, which indicates that adsorption occurs on the surface of the adsorbent and can be applied to both physical and chemical adsorption. The exact expression is given in Equation (10).

$$q_e = K \cdot C_e^{\frac{1}{n}} \quad (10)$$

where n and K represent the Freundlich empirical constants that evaluate the adsorption intensity and adsorption capacity ($(\text{mg}^{-1} (\text{L mg}^{-1})^{1/n})$). The K value can indicate the strength of the adsorption capacity. The n value can indicate the strength of adsorption and the inhomogeneity of the adsorbent.

Figure 8 shows the nonlinear curve fitting results of the experimental data using Langmuir and Freundlich isothermal adsorption models. The fitted parameters are shown in Table 4. The results show that the R^2 value of the Langmuir model is higher than that of the Freundlich model, and the q_e value of the Langmuir model is $0.43476 \text{ mg g}^{-1}$, consistent with the experimental results. The Langmuir isothermal model is more suitable for fitting Fe(II) adsorption on coal samples, which can be regarded as the adsorption of Fe(II) on coal samples as monomolecular layer adsorption. By comparing it with the reported literature on the subject, the adsorption obtained by modeling in this work is better [29]. It has some potential for treating heavy metals in coal mine water.

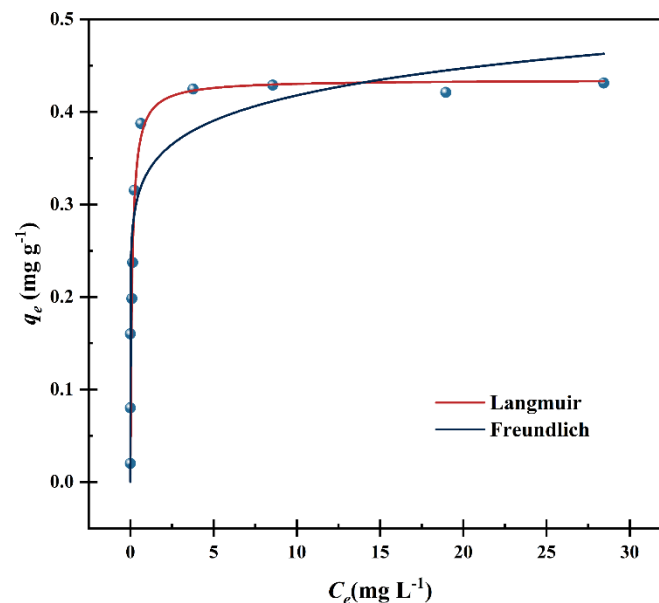


Figure 8. Langmuir and Freundlich isothermal adsorption fitting curves of Fe(II) adsorption by coal samples.

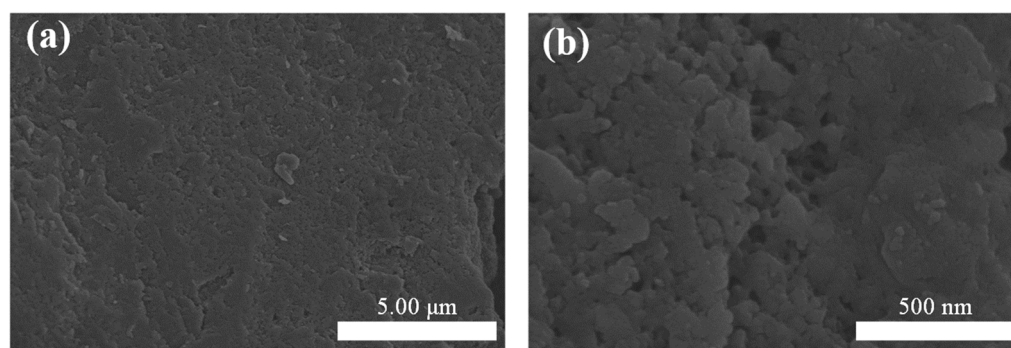
Table 4. Fitting parameters of Langmuir and Freundlich models for Fe(II) adsorption by coal samples.

Sample	Langmuir			Freundlich		
	q_e (mg g ⁻¹)	b (L mg ⁻¹)	R^2	k	n	R^2
Noncaking coal	0.43476	9.45578	0.855	0.33353	10.22959	0.76922

3.7. Discussion of the Adsorption Mechanism

3.7.1. Microstructural Changes

Figure 9 shows SEM images of the coal samples after adsorption. The surfaces became rough and a small amount of crumbly particles appeared in the local areas at the observation scale of 5.00 μm , and the crumbly particles could be seen in a scale-like random distribution at the observation scale of 500 nm. The heavy metal ions in solution were adsorbed on the surface of the coal samples as small particles of sediments through adsorption on the surface pores or ligand reaction with the metal ions.

**Figure 9.** SEM images of coal samples after adsorption of Fe(II). (a) At 5.00 μm scale; (b) At 500 nm scale.

3.7.2. Changes in Elemental and Mineral Composition

The adsorbed coal samples were subjected to EDX assay to investigate the changes in the constituent elements of the coal samples after adsorption. The adsorbed coal samples were taken from the isothermal adsorption test group after adsorption in Fe(II) solutions with initial concentrations of 4 mg L⁻¹, 12 mg L⁻¹, 20 mg L⁻¹, and 30 mg L⁻¹. Considering the limitation of the shallow depth of X-ray penetration in the EDX assay [30], the results were used only for qualitative analysis. Elemental Fe was detected at 0.739 keV and 6.414 keV, which indicates that Fe(II) in solution was adsorbed onto the surface of the coal sample particles. Table 5 shows the changes in the constituent elements and contents of the coal samples before and after adsorption. From Table 5, it can be seen that the Fe element and its content in the constituent elements of the coal samples increased gradually after the adsorption of Fe(II).

Table 5. Changes in composition and content in the coal before and after adsorption.

Element	C	O	Al	Si	S	Ca	Fe
Before adsorption	77.18%	19.62%	0.13%	0.16%	0.11%	2.80%	0.00%
4 mg L ⁻¹	79.15%	19.14%	0.17%	0.13%	0.09%	1.23%	0.09%
12 mg L ⁻¹	79.40%	18.36%	0.16%	0.21%	0.09%	1.66%	0.12%
20 mg L ⁻¹	79.39%	19.22%	0.20%	0.15%	0.13%	0.76%	0.15%
30 mg L ⁻¹	80.35%	18.22%	0.14%	0.19%	0.15%	0.71%	0.24%

The X-ray diffraction (XRD) patterns of the coal samples after adsorption are shown in Figure 10, where 4 mg L⁻¹, 12 mg L⁻¹, 20 mg L⁻¹, and 30 mg L⁻¹ represent the concentrations of the initial solutions in the isothermal adsorption experimental group. By

comparing the XRD patterns of the samples before and after adsorption, the positions of the absorption peaks did not change, which indicated that the mineral composition and crystal structure in the coal were not damaged. The intensity of the absorption peaks at 29.5° and 43.2° showed a small decrease, which indicated that a small number of calcite crystals were decomposed. Since the isothermal adsorption experiment was conducted in a weakly acidic environment ($\text{pH} = 6$), the small number of calcite crystals in the coal samples reacted with H^+ in the solution, which led to the decrease in calcite content. The decrease in the elemental Ca content in the EDX results was corroborated by the decrease in calcite content.

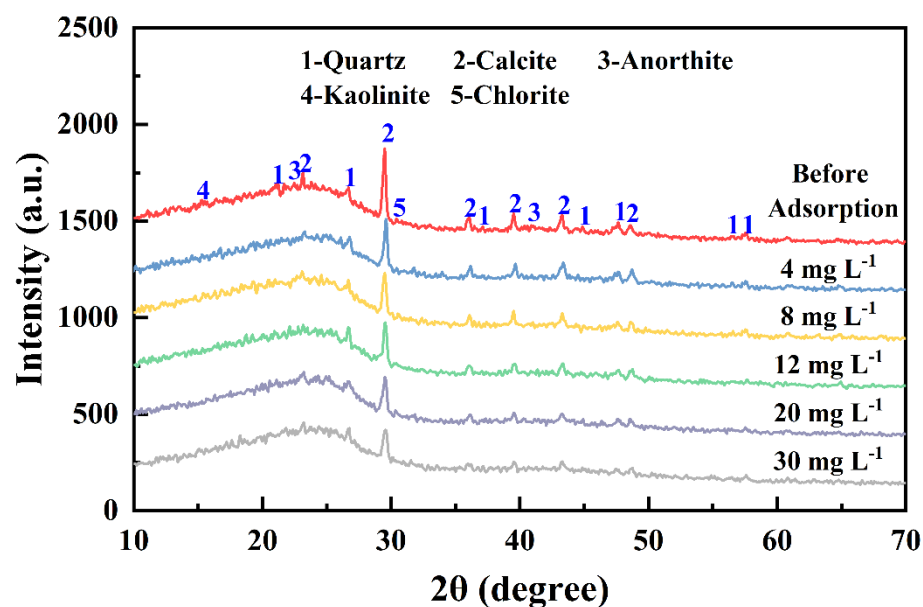


Figure 10. XRD patterns of coal samples before and after adsorption.

3.7.3. FT-IR Analysis

The Fourier transform infrared spectra (FT-IR) of the coal samples before and after the adsorption of Fe(II) are shown in Figure 11. The adsorbed coal samples were taken from the isothermal adsorption experiments after adsorption in a solution with an initial concentration of 30 mg L^{-1} . The intensities of the absorption peaks at 1348 cm^{-1} , 1398 cm^{-1} , 1600 cm^{-1} , and $2600\text{--}3600 \text{ cm}^{-1}$ wave numbers of the coal samples were significantly reduced after adsorption, which indicated that there was a shedding of the internal functional groups of the coal samples after adsorption.

According to the literature [31,32], the FT-IR spectra of coal samples can generally be divided into four subzones, which are the aryl ring substitution zone between 900 and 700 cm^{-1} , the oxygen-containing functional group zone between 1800 and 1000 cm^{-1} , the aliphatic zone between 3000 and 2800 cm^{-1} , and the hydrogen bonding zone between 3600 and 3000 cm^{-1} . Since the aliphatic and hydrogen bonded regions of the coal samples in this study interfered with each other and the range of the aliphatic region was enlarged, the infrared spectra in the range of $2600\text{--}3600 \text{ cm}^{-1}$ were combined into a single interval for analysis in order to ensure the accuracy of the split-peak fitting. The Gaussian function was used to fit the peaks in each interval of the coal samples before and after adsorption to obtain the absorption peak positions, peak area ratios, and area ratio parameters of the major functional groups. The results of peak fitting for each interval of coal samples before and after adsorption are shown in Figure 12.

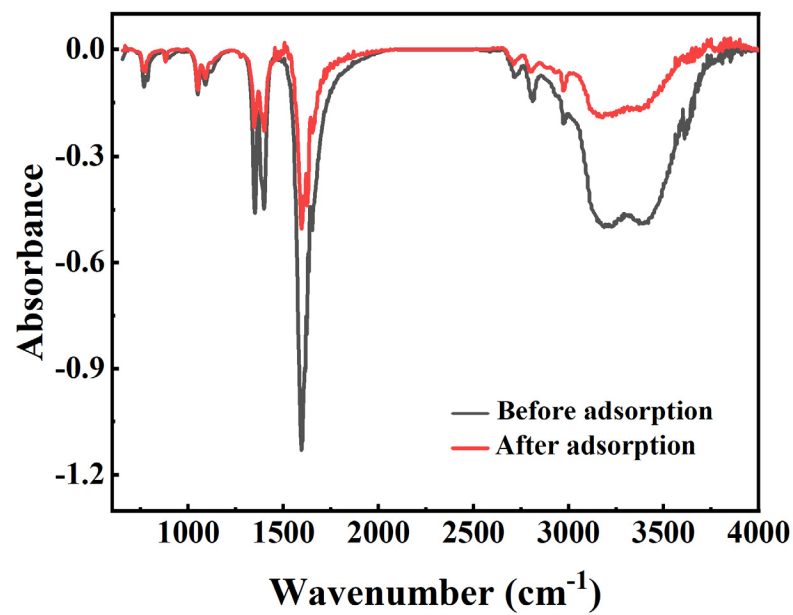


Figure 11. FT-IR spectra of coal samples before and after Fe(II) adsorption by coal samples.

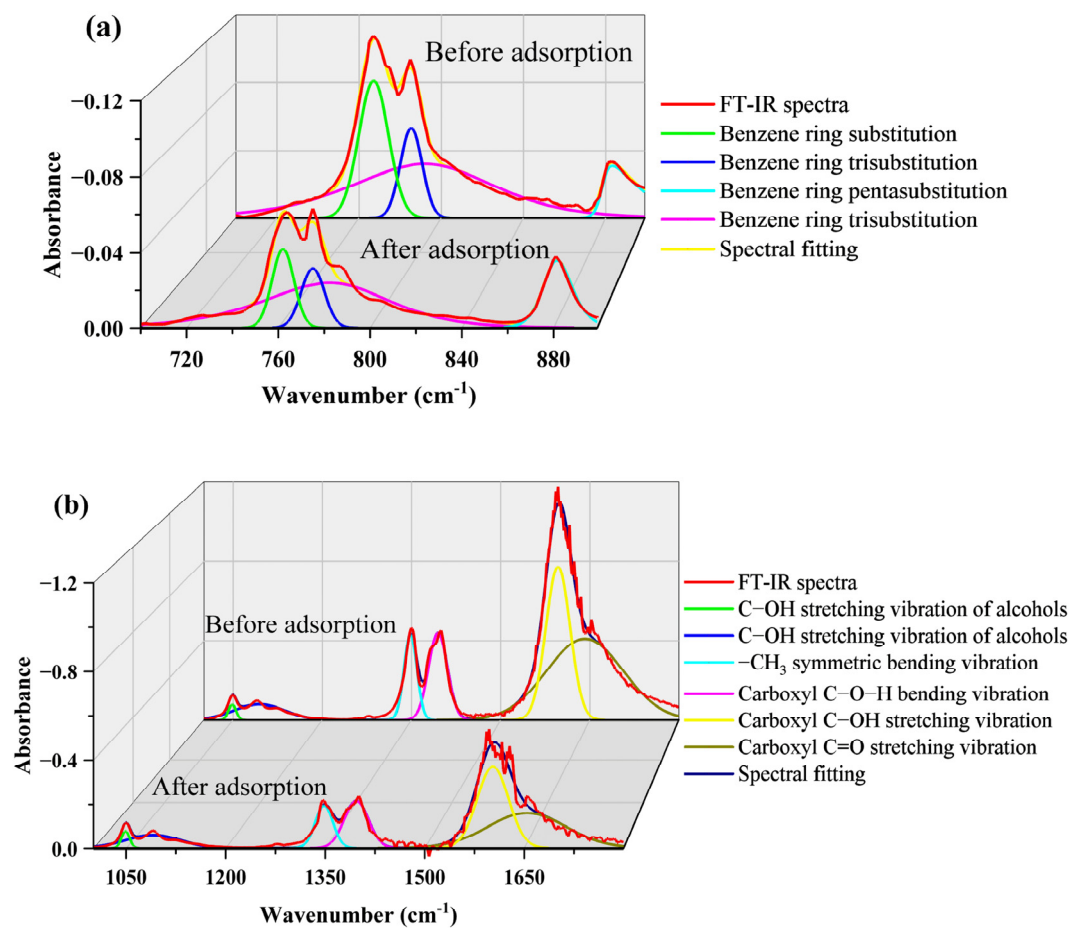


Figure 12. Cont.

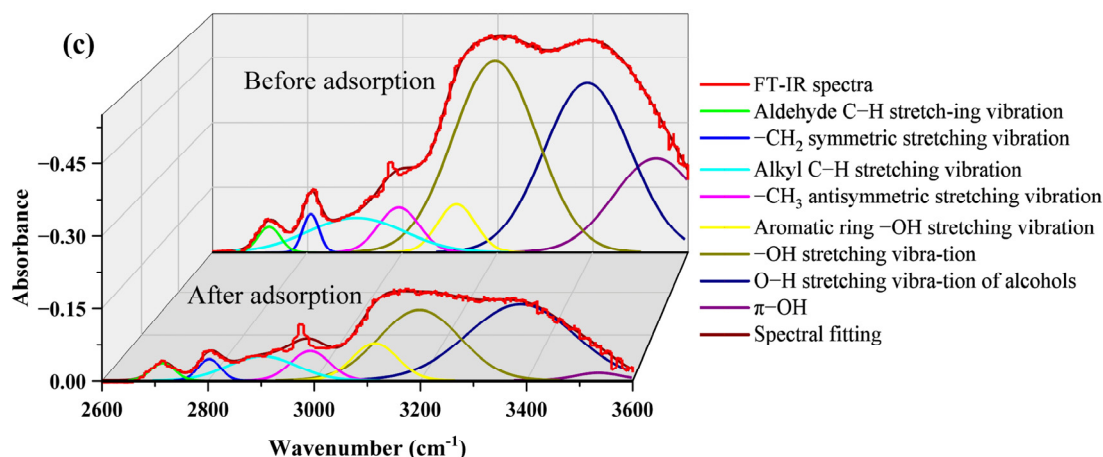


Figure 12. Fitted curves of different stages of peak splitting of FT-IR of nonstick coal before and after adsorption: (a) aryl ring substituent region; (b) oxygen-atom-containing functional group region; (c) aliphatic and hydrogen bonding region.

Figure 12a shows the peak fitting of coal samples before and after adsorption in the aromatic ring substitution region ($700\text{--}900\text{ cm}^{-1}$). Both can be fitted with four subpeaks, which are the benzene ring monosubstitution near 767 cm^{-1} , two benzene ring trisubstitutions near $770\text{--}790\text{ cm}^{-1}$, and benzene ring pentasubstitution near 883 cm^{-1} . The results of the fitting parameters of each subpeak are shown in Table 6, which shows that the peak position of the benzene ring trisubstituted in the coal samples after adsorption decreased by 10 cm^{-1} . At the same time, the peak positions of the rest of the functional groups remained almost unchanged. The proportion of benzene ring trisubstitution was the highest in the coal samples before adsorption, followed by benzene ring monosubstitution. The highest proportion of benzene ring trisubstitution, followed by benzene ring pentasubstitution, was found in the functional groups of the post-adsorption coal samples. Although the positions and percentages of some functional groups were changed, the overall content of functional groups decreased insignificantly, indicating that the adsorption of Fe(II) was less affected by the functional groups in this region.

Table 6. Fitting parameters of aromatic ring region ($700\text{--}900\text{ cm}^{-1}$) in FT-IR spectrum.

Number	Functional Group	Before Adsorption			After Adsorption		
		Peak Position (cm^{-1})	Peak Area	Area Ratio (%)	Peak Position (cm^{-1})	Peak Area	Area Ratio (%)
1	Benzene ring substitution	767	1.48	26.24	764	0.50	15.59
2	Benzene ring trisubstitution	785	0.71	12.65	775	0.40	12.51
3	Benzene ring trisubstitution	789	2.89	51.28	778	1.73	53.56
4	Benzene ring pentasubstitution	883	0.55	9.83	882	0.59	18.34

Figure 12b shows the peak fitting results of coal samples before and after adsorption in the oxygen-containing functional group region ($1800\text{--}1000\text{ cm}^{-1}$). Both can be fitted with six subpeaks, which are the C-OH stretching vibrations near 1049 and 1094 cm^{-1} for alcohols, the $-\text{CH}_3$ symmetric bending vibration near 1348 cm^{-1} , the C-O-H in-plane bending vibration, the C-OH stretching vibration near 1597 cm^{-1} , and the C=O stretching vibration near 1648 cm^{-1} . The results of the fitted parameters of the individual subpeaks are shown in Table 7, which shows that the positions of the subpeaks before and after adsorption were almost unchanged, and the order of the areas of the individual subpeaks did not change. The peak areas of individual subpeaks in the coal samples after adsorption were significantly reduced: the carboxyl groups ($-\text{COOH}$) at 1602 cm^{-1} and 1654 cm^{-1} . The carboxyl peak area of the coal sample after adsorption was 43% of that before adsorption, which indicates that the adsorption of Fe(II) reduced the carboxyl group content.

Table 7. Peak fitting parameters of FT-IR spectrum in oxygen-containing functional group region (1000–1800 cm^{-1}).

Number	Functional Group	Before Adsorption			After Adsorption		
		Peak Position (cm^{-1})	Peak Area	Area Ratio (%)	Peak Position (cm^{-1})	Peak Area	Area Ratio (%)
1	C–OH stretching vibration of alcohols	1049	1.31	0.91	1049	1.22	1.77
2	C–OH stretching vibration of alcohols	1094	8.65	5.90	1090	6.09	8.83
3	–CH ₃ symmetric bending vibration	1348	11.80	8.17	1348	6.53	9.47
4	Carboxyl C–O–H bending vibration	1395	17.52	12.14	1396	9.80	14.21
5	Carboxyl C–OH stretching vibration	1597	39.49	27.36	1602	21.92	31.77
6	Carboxyl C=O stretching vibration	1648	66.19	45.52	1654	23.42	33.95

Figure 12c shows the results of peak fitting in the aliphatic region (2600–3000 cm^{-1}) and hydrogen bonding region (3000–3600 cm^{-1}) for the coal samples before and after adsorption. Both can be fitted with six subpeaks. The subpeaks in the aliphatic region are aldehyde C–H stretching vibration near 2718 cm^{-1} , –CH₂ symmetric stretching vibration near 2806 cm^{-1} , alkyl C–H stretching vibration near 2902 cm^{-1} , and CH₃ antisymmetric stretching vibration near 2992 cm^{-1} . The subpeaks in the hydrogen bonding region are the aryl ring –OH stretching vibration near 3113 cm^{-1} , the –OH stretching vibration near 3194 cm^{-1} , the O–H stretching vibration of the alcohol near 3388 cm^{-1} , and the π -. The results of the fitting parameters for each subpeak are shown in Table 8. Table 8 shows no significant change in the position of the functional groups in the aliphatic region. In contrast, there is a decrease in the alkyl functional group, suggesting a detachment of the CH₃/CH₂ aliphatic chain during the adsorption process. Similarly, the positions of functional groups in the hydrogen bonding region did not change. In contrast, the peak areas of the –OH functional groups at 3194 and 3388 decreased significantly, indicating the presence of –OH shedding during the adsorption of Fe(II).

Table 8. Fitting parameters for aliphatic region (2600–3000 cm^{-1}) and hydrogen bond region (3000–3600 cm^{-1}) in FT-IR spectrum.

Number	Functional Group	Before Adsorption			After Adsorption		
		Peak Position (cm^{-1})	Peak Area	Area Ratio (%)	Peak Position (cm^{-1})	Peak Area	Area Ratio (%)
1	Aldehyde C–H stretching vibration	2718	3.56	1.30	2714	2.11	2.20
2	–CH ₂ symmetric stretching vibration	2806	3.86	1.41	2802	2.40	2.51
3	Alkyl C–H stretching vibration	2902	20.39	7.45	2902	8.29	8.67
4	–CH ₃ antisymmetric stretching vibration	2992	11.21	4.09	2992	5.69	5.96
5	Aromatic ring –OH stretching vibration	3113	11.15	4.07	3114	8.32	8.70
6	–OH stretching vibration	3194	98.00	35.79	3197	28.07	29.36
7	O–H stretching vibration of alcohols	3388	88.06	32.16	3388	39.19	40.99
8	π –OH	3533	37.60	13.73	3534	1.55	1.62

From the adsorption kinetic analysis and isothermal adsorption results, it is clear that the adsorption of Fe(II) by the nonstick coal is dominated by chemisorption in the monomolecular layer. Fine particulate matter precipitation was generated according to the microscopic surfaces of the coal samples after adsorption. The elemental analysis of the coal samples after adsorption proved the adsorption of Fe(II) to the particle surfaces of the coal samples. Meanwhile, the FT-IR quantitative analysis showed that many hydroxyl functional groups were shed in the adsorbed coal samples. In the hydroxyl group, losing a proton to a hydroxyl radical ion (OH⁻) is easy under acidic conditions. Since Fe(II) has a reducing property, it can easily complex with OH⁻. Therefore, nonstick coal achieves adsorption of Fe(II) under laboratory conditions at room temperature (25 °C) in near-neutral (pH = 5–7) conditions.

4. Conclusions

Aiming at the problem of the high heavy metal content in mine water, which leads to a low reuse rate for mine water, in this research, the Fe(II) adsorption potential was

investigated using the nonstick coal in a mine in western China. The following conclusions were drawn under laboratory studies:

(1) The adsorption amount and unit removal rate decreased gradually with the increase in the solid–liquid ratio. The adsorption of nonstick coal was better in the range of pH = 5~7. The adsorption process of the coal samples was heating, absorbing, and warming up, which was favorable for adsorption. The quasi-secondary kinetic model and the Langmuir model fitted the adsorption kinetic curves and isothermal adsorption curves well, which indicated that the chemical adsorption mainly occurred in the monomolecular layer.

(2) After the adsorption, tiny particles of precipitate were generated on the surface of the coal samples, and the content of Fe increased. Meanwhile, the quantitative analysis results of FT-IR showed that the -OH functional groups were significantly reduced, and it was easy for them to lose their protons to hydroxyl ions (OH⁻) under acidic conditions, which complexed with Fe(II) to produce a precipitate.

Author Contributions: Z.S. and C.W. conceived and designed the experimental program; C.W., Z.S., F.W. and J.S. (Jialong Sun) conducted the laboratory experiments; C.W., Z.S. and F.W. organized and analyzed the experimental data; Y.X., C.W. and J.S. (Jinhang Shen) performed the theoretical model validation; Z.S. and C.W. wrote the first draft of the paper; C.W. helped Z.S. to revise the first draft. All authors have read and agreed to the published version of the manuscript.

Funding: This research was funded by the Science and Technology Innovation Special Fund of the Jiangsu Provincial Science and Technology Department (approval no. BK20220024, project no. 2022-12460).

Data Availability Statement: No new data were created or analyzed in this study. Data sharing is not applicable to this article.

Conflicts of Interest: The authors declare that they have no conflicts of interest.

References

1. Xiao, W. China Coal Market Analysis 2022 and Outlook 2023. *China Steel Focus* **2023**, *4*, 41–44.
2. Yao, Q.L.; Tang, C.J.; Liu, Z.C. Discussion on coal and water co-mining in ecologically fragile mining areas in western China. *Coal Sci. Technol.* **2021**, *49*, 225–232. [[CrossRef](#)]
3. Wang, S.M.; Duan, Z.H.; Ma, L.; Zhang, Y.P. Research status and future trends of geological assurance technology for coal green development in Western China. *Coal Sci. Technol.* **2019**, *47*, 1–6. [[CrossRef](#)]
4. Gu, D.Z. Theory framework and technological system of coal mine underground reservoir. *J. China Coal Soc.* **2015**, *40*, 239–246. [[CrossRef](#)]
5. Fan, L.; Ma, X. A review on investigation of water-preserved coal mining in western China. *Int. J. Coal Sci. Technol.* **2018**, *5*, 411–416. [[CrossRef](#)]
6. He, X.W.; Zhang, X.H.; Li, F.Q.; Zhang, C.H. Comprehensive utilization system and technical innovation of coal mine water resources. *Coal Sci. Technol.* **2018**, *46*, 4–11. [[CrossRef](#)]
7. Sun, Y.J.; Chen, G.; Xu, Z.M.; Yuan, H.Q.; Zhang, Y.Z.; Zhou, L.J.; Wang, X.; Zhang, C.X.; Zheng, J.M. Research progress of water environment, treatment and utilization in coal mining areas of China. *J. China Coal Soc.* **2020**, *45*, 304–316. [[CrossRef](#)]
8. Song, W.; Zhou, P. Characteristic and Processing Engineering Practice of Acidity Mine Water Containing Fe and Mn. *J. Guizhou Univ. (Nat. Sci.)* **2010**, *27*, 129–132. [[CrossRef](#)]
9. Zhou, L.; Yi, T.; Zheng, S.S.; Zhu, X.Q.; Wu, J.F. Experimenta simulation on the electrochemica mechanism of iron pollution from “dua-source” in closed coal mine water. *Coal Sci. Technol.* **2023**, *2023*, 10. [[CrossRef](#)]
10. Jiang, B.B.; Liu, S.Y.; Ren, J.; Zheng, R.F.; Chen, M.Y.; Yu, Y.; Zhang, K. Purification effect of coal mine groundwater reservoir on mine water containing orgqanic compounds and heavy metals in different occurrence forms. *Coal Eng.* **2020**, *52*, 122–127.
11. Pondja, E.A.; Bashitialshaaer, R.; Persson, K.M.; Matsinhe, N.P.; Kanan, S. Bioadsorbents of heavy metals from coal mines area in Mozambique. *Cogent Environ. Sci.* **2017**, *3*, 1355088. [[CrossRef](#)]
12. Zhao, H.J. Wastewater Treatment by Adsorption. *Guangdong Chem. Ind.* **2016**, *43*, 128–129.
13. Lin, X.F. Removal of Heavy Metals from Acid Drainage by Pig Bone Meal. Master’s Thesis, South China University of Technology, Guangzhou, China, 2018.
14. Liu, H.L.; He, L.H.; Zhao, Y. Research Progress in Adsorption Materials for Heavy Metals. *J. Salt Sci. Chem. Ind.* **2023**, *45*, 437–444. [[CrossRef](#)]
15. Jochová, M.; Puncochár, M.; Horáček, J.; Stamberg, K.; Vopálka, D. Removal of heavy metals from water by lignite-based sorbents. *Fuel* **2004**, *83*, 1197–1203. [[CrossRef](#)]

16. Bezuglova, O.S.; Gorbov, S.N.; Tischenko, S.A.; Shimko, A.E. Use of brown coal as a detoxifier of soils contaminated with heavy metals. *J. Geochem. Explor.* **2018**, *184*, 232–238. [[CrossRef](#)]
17. Yao, Q.L.; Wang, W.N.; Xia, Z.; Zhu, L.; Wang, A.; Yu, L.Q. Adsorption characteristics of Mn(II) on sandy mudstone and fine sandstone of coal measures. *J. China Univ. Min. Technol.* **2020**, *49*, 411–418. [[CrossRef](#)]
18. Ma, X.; Wang, H.K.; Li, L.; Zhon, X.J.; Wu, H.T. Adsorption Characteristics and Mechanisms of Cr(VI) on Coal Gangue-Chitosan Particulate Composite Material. *Environ. Sci. Technol.* **2021**, *44*, 68–75. [[CrossRef](#)]
19. Xuan, Y.W.; Wu, W. Determination of Iron in the Industrial Waste Water by Spectrophotometry. *Chin. J. Spectrosc. Lab.* **2011**, *28*, 1560–1563. [[CrossRef](#)]
20. Wang, W.M.; Wang, Z.M.; Chen, X.; Long, F.; Lu, S.F.; Liu, G.H.; Tian, W.C.; Su, Y. Fractal nature of porosity in volcanic tight reservoirs of the San tanghu Basin and its relationship to pore formation processes. *Fractals Interdiscip. J. Complex Geom. Nat.* **2018**, *26*, 1840007.
21. Yi, G.X.; Wang, N.; Xu, H.; Ou, R. The Formation Mechanism and Major Treatment Technology of Acidic Mine Water. *Environ. Sci. Manag.* **2008**, *9*, 100–102. [[CrossRef](#)]
22. Wu, D.S. Research on treatment of acid mine water with high salty and high iron. *Coal Sci. Technol.* **2008**, *8*, 110–112. [[CrossRef](#)]
23. Xiong, Y.; Xu, J.; Shan, W.J.; Lou, Z.N.; Fang, D.W.; Zang, S.L.; Han, G.X. A new approach for rhenium(VII) recovery by using modified brown algae *Laminaria japonica* adsorbent. *Bioresour. Technol.* **2013**, *127*, 464–472. [[CrossRef](#)]
24. Peniche-Covas, C.; Alvarez, L.W.; Argüelles-Monal, W. The adsorption of mercuric ions by chitosan. *J. Appl. Polym. Sci.* **2010**, *46*, 1147–1150. [[CrossRef](#)]
25. Lagergren, S. Zur theorie der sogenannten adsorption gelöster stoffe. *K. Sven. Vetenskapsakademiens. Handl.* **1898**, *24*, 1–39.
26. Ho, Y.S.; Kay, M. Pseudo-second order model for sorption processes. *Process Biochem.* **1999**, *34*, 451–465. [[CrossRef](#)]
27. Langmuir, I. The constitution and fundamental properties of solids and liquids. part I. solids. *J. Am. Chem. Soc.* **1916**, *38*, 2221–2295. [[CrossRef](#)]
28. Freundlich, H. Über die Adsorption in Lösungen. *Z. Für Phys. Chem.* **1907**, *57*, 385–470. [[CrossRef](#)]
29. Yao, Q.-L.; Xia, Z.; Tang, C.-J.; Zhu, L.; Wang, W.-N.; Chen, T.; Tan, Y.-M. Characteristics of Heavy Metal Ion Adsorption by Silty Mudstones in Coal Mine Goafs. *Geofluids* **2020**, *2020*, 8560151. [[CrossRef](#)]
30. Chai, X.; Mi, H.; He, C. Principles and maintenance of scanning electron microscope and X-ray energy spectrometer. *Autom. Instrum.* **2018**, *523*, 192–194.
31. Liang, C.H.; Liang, W.Q.; Li, W. Functional groups of different coal ranks based on infrared spectroscopy. *Coal Sci. Technol.* **2020**, *48*, 182–186.
32. Li, X.Z.; Zhang, M.Q.; Yang, Z.B.; Liu, Y.; Ding, C.; Huang, G. Effect of fault structure on the structure and oxidative spontaneous combustion characteristics of coal. *J. China Coal Soc.* **2023**, *48*, 1246–1254. [[CrossRef](#)]

Disclaimer/Publisher’s Note: The statements, opinions and data contained in all publications are solely those of the individual author(s) and contributor(s) and not of MDPI and/or the editor(s). MDPI and/or the editor(s) disclaim responsibility for any injury to people or property resulting from any ideas, methods, instructions or products referred to in the content.